Controlled morphology synthesis of nanostructured β-AlF3– x(OH)x with tunable specific surface area

Valentine Camus-Génot, Amandine Guiet, Jérôme Lhoste, Franck Fayon, Monique Body, Stéphanie Kodjikian, Romain Moury, Marc Leblanc, Jean-Louis Bobet, Christophe Legein, et al.

Controlled Morphology Synthesis of Nanostructured β-$AlF_{3-x}(OH)_x$ with Tunable Specific Surface Area

Valentine Camus-Génot,[1] Amandine Guiet,[1] Jérôme Lhoste,[,1] Franck Fayon,[2] Monique Body,[1] Stéphanie Kodjikian,[1,†] Romain Moury,[1] Marc Leblanc,[1] Jean-Louis Bobet,[3] Christophe Legein,[*,1] Vincent Maisonneuve[1]*

[1]Institut des Molécules et Matériaux du Mans (IMMM), UMR 6283 CNRS, Le Mans Université, Avenue Olivier Messiaen, 72085 Le Mans Cedex 9, France

[2] CNRS, CEMHTI UPR3079, Université d'Orléans, 1D Avenue de la Recherche Scientifique, F-45071 Orléans, France

[3] CNRS, Université Bordeaux, Bordeaux INP, ICMCB UMR 5026, Pessac, Bordeaux F-33600, France

KEYWORDS. Hexagonal Tungsten Bronze (HTB), Aluminium hydroxyfluoride, β-$AlF_{3-x}(OH)_x$, microwave-assisted solvothermal synthesis, nanoparticles, high specific surface area, ^{27}Al and ^{19}F solid state NMR, gas adsorption.

Abstract

In this work, the synthesis of β-$AlF_{3-x}(OH)_x$ nanoparticles with very high specific surface area (SSA) using a microwave-assisted solvothermal process is reported. The influence of the synthesis parameters on the morphology and SSA was investigated and the nature of the solvent is shown to have the greatest impact. Five samples prepared using different solvent mixtures were deeply characterised by thermogravimetric analysis (TGA), N_2 sorption, powder X-ray diffraction, transmission electron microscopy (TEM) and ^{19}F and ^{27}Al high field solid-state NMR. Their SSA range from 25 to 345 $m^2.g^{-1}$ with an associated OH content slightly increasing from ≈ 16% ($AlF_{2.52}(OH)_{0.48}$) to ≈ 19% ($AlF_{2.42}(OH)_{0.58}$), as estimated by TGA and ^{27}Al high field solid state NMR. Compared to previous reference work [Dambournet *et al.* Chem. Mater. 20, 1459 (2008)], β-$AlF_{3-x}(OH)_x$ nanoparticles with SSA up to four times larger were obtained. TEM revealed the formation of hollow nanostructures except when the surface exceeds 300 $m^2.g^{-1}$, in which case isolated nanoparticles are observed. The sample with the highest SSA also displaying an appealing cumulative pore volume of 0.060 $cm^3.g^{-1}$, its hydrogen adsorption capability was evaluated to show that β-$AlF_{3-x}(OH)_x$ nanoparticles have a potential interest for hydrogen storage applications.

Introduction

In the last decades, a lot of work has been devoted to the synthesis and characterization of metal fluorides due to their physical and chemical properties for many potential applications in catalysis, optics, energy conversion and high T_c superconductors.[1–4] Among them, aluminum trifluoride AlF_3 is widely studied for applications such as cathode material coatings for batteries,[5,6] highly reflective mirrors[7] and optics.[8] Due to its high Lewis acidity, AlF_3 is also of great interest as heterogeneous catalyst for reactions such as halogen exchange,[9] fluorination, dehydrofluorination of hydrofluorocarbons[10–12] or hydrolysis of NF_3.[13]

AlF_3 presents five allotropic structures depending on the packing of the AlF_6 octahedral units. The thermodynamically stable α-AlF_3 adopts the VF_3-type structure (rhombohedral, space group (SG): *R*-3*c* (167))[14] and exhibits a dense network with narrow cavities (**Figure S1**) while the β-[15] and η-[16] AlF_3 phases are built up from corner-sharing octahedra to form open framework structures. β-AlF_3 is closely related to the hexagonal tungsten bronze (HTB) structure (orthorhombic, SG: *Cmcm* (63), **Figure 1**) and the η-phase adopts a cubic pyrochlore structure (cubic, SG: $Fd\bar{3}m$ (227), **Figure S1**). Diffusion channels are observed in six equivalent [110] directions for the pyrochlore structure and along the *c*-axis in the HTB structure. Water molecules can be located in these hexagonal tunnels and can be eliminated with an appropriate thermal treatment at temperatures from 110 to 380°C.[17]

Nanosized crystalline β-$AlF_{3-x}(OH)_x$ can be prepared by several different synthesis approaches such as sol-gel fluorolytic process,[18] non-aqueous route,[19] thermal decomposition of α-NH_4AlF_4,[20] dehydration of α-$AlF_3 \cdot H_2O$,[21] thermal treatment of α-$AlF_3 \cdot 3H_2O$ nanorods in air atmosphere,[22] oxidative decomposition of $N_2H_6AlF_5$,[23] plasma-fluorination syntheses[24] or hydro(solvo)thermal synthesis.[25] The microwave-assisted solvothermal synthesis method

developed by Demourgues *et al.* was shown to be very efficient to prepare rapidly pure nanostructured hydroxyfluorides $AlF_{3-x}(OH)_x \cdot nH_2O$.[26,27] These authors also showed the relationships between the OH rate inside the anion framework, strongly dependent of the [HF]/[Al] precursor molar ratio, and the nature of the obtained allotropic form. For [HF]/[Al] = 3, β-$AlF_{3-x}(OH)_x \cdot nH_2O$ is obtained from a mixture of aluminium nitrate, water/isopropanol (^{i}PrOH) solvent and aqueous HF. After tuning the water/isopropanol ratio, the largest SSA reached by these authors was 85 $m^2.g^{-1}$ for $AlF_{2.6}(OH)_{0.4} \cdot nH_2O$ nanoparticles with an average size of 15 nm.

Herein, we report on our quest to significantly increase the SSA of pure β-$AlF_{3-x}(OH)_x \cdot nH_2O$ nanoparticles, by optimizing the conditions of the microwave-assisted solvothermal syntheses. Nanoparticle sizes, specific surface areas and pore volumes were estimated by Powder X-Ray Diffraction (PXRD), N_2 sorption and Transmission Electron Microscopy (TEM) analyses. The influence of the solvent composition on the nanostructured morphology was also studied. Thermogravimetric analysis (TGA) and high-field solid-state nuclear magnetic resonance (NMR) spectroscopy were used to determine the β-$AlF_{3-x}(OH)_x \cdot nH_2O$ formulations.

Surprisingly, whereas fluorous metal-organic frameworks (FMOFs) possess higher gas affinity and selectivity compared to their non-fluorous counterparts,[28] fluorinated inorganic compounds have never been considered for gas storage. Considering their high pore densities related to large channels, the β- and η- phases of AlF_3 present *a priori* favourable properties for gas storage applications. The β-$AlF_{3-x}(OH)_x$ sample presenting the largest SSA and displaying a cumulative pore volume of 0.060 $cm^3.g^{-1}$ was thus investigated for hydrogen adsorption application.

Experimental section

Synthesis procedure. Aluminium nitrate ($Al(NO_3)_3 \cdot 9H_2O$), supplied by Alfa Aesar, was employed as the aluminium precursor and used without any prior purification. Solvents such as ^{i}PrOH, ethanol (EtOH) and methanol (MeOH) were used as supplied by Sigma-Aldrich. Hydrofluoric acid solution (HF_{aq}, 40%) was provided by Riedel De Haen (Paris, France). *[Caution: HF is a highly corrosive acid and proper protective equipments are mandatory.]*

Synthesis of β-$AlF_{3-x}(OH)_x$ involves two consecutive steps: chemical reaction followed by a drying process. The microwave (MW) route is based on two heating mechanisms (dipolar polarization and ionic conduction) and its major advantage is to heat directly the core of the solution. Significant improvements of the reaction kinetics are observed and the control of the germination-growth process, and thus the SSA of the obtained material, is possible by tuning the synthesis conditions. All syntheses of β-AlF_3 were carried out from $Al(NO_3)_3 \cdot 9H_2O$ and $HF_{aq.}$ (40%) with a ratio F/Al fixed to 3 and with the same volume of solvent (20 mL). First, $Al(NO_3)_3 \cdot 9H_2O$ and $HF_{aq.}$ are loaded in a PTFE (polytetrafluoroethylene) lined autoclave. After a quick manual stirring, the solvent is added and the solvothermal reaction is performed in a microwave oven (Mars 5 CEM). Two drying methods were tested: the classical method that consists of a simple filtering at room temperature and MW drying that involves a fast solvent evaporation by MW heating at 100 °C during 15 min under primary vacuum. The resulting powders are washed with ethanol and acetone, dried at room temperature, sieved (125 μm) and finally outgassed at 150 °C, during 8 h, under secondary vacuum.

The statistical Design of Experiment method (DoE[29]) was applied to determine the influence of eight factors on the SSA (**Table S1**). The specific DoE software MODDE 8.0 (from Umetrics,

Umea, Sweden) was used to build the design and perform mathematical and statistical analyses of the collected data.

Powder X-Ray Diffraction analysis. Data were collected in θ/2θ geometry using a Panalytical X'pert MPDPRO diffractometer (Cu-Kα radiation) in the 2θ range 10 to 100° with a step size of 0.033° and a total duration of 3 h. The instrumental resolution function of the diffractometer was extracted from the PXRD pattern of LaB_6 NIST SRM 660. All PXRD patterns were analysed by the Rietveld method[30] with the Fullprof program.[31] As the electronic weight is the same for F and OH yielding very similar X-ray scattering factors, the OH content was set to zero (x = 0) in the structural model of β-$AlF_{3-x}(OH)_x$ (ICSD-202681, AlF_3, orthorhombic system, SG: *Cmcm*, *a* = 6.931 Å, *b* = 12.002 Å, *c* = 7.134 Å, V = 593.4 $Å^3$).[15] The Al-F distances were constrained. The XRD line broadening contribution due to the nanometric size of the sample was calculated by using Thompson–Cox–Hastings pseudo-Voigt function[32] that includes size and strain-broadening terms for both Lorentzian and Gaussian components. The two parameters (Y and F) of the Lorentzian component of this function were refined to calculate the apparent crystallite size <L> using the Langford's method.[33] The diameter D_{XRD} of the spherical particles is related to <L> by the following formula $D_{XRD} = 4/3 \times <L>$. The overall isotropic displacement factor (Bov) and the parameter G1 of the preferred orientation function were refined (March's function). Crystal data, data collection and structure refinement details are given as SI (**Table S2**).

Thermal measurements. Thermogravimetric analyses were performed with a TA Instruments SDT-Q600 under nitrogen atmosphere (heating rate 10°C/min). Thermodiffraction patterns were collected on a Panalytical X'Pert Pro diffractometer, employing Cu K*α* radiation, equipped with a RTMS X'Celerator detector and an Anton Paar XRK 900 high temperature furnace. The samples

were heated under nitrogen gas from room temperature to 700°C at a heating rate of 10°C.min^{-1}. PXRD patterns were collected at 50°C intervals in the 10–60° 2θ range with a scan time of 15 min.

Transmission Electronic Microscopy (TEM). TEM images were obtained with a 200 kV JEOL 2010 microscope. A small quantity of powder was suspended in ethanol and then dispersed using an ultrasonic bath; one droplet was deposited on a holey amorphous carbon film supported by a copper grid, then dried.

BET measurements. Prior to the N_2 adsorption measurements, the samples were degassed under primary vacuum, at 150°C for 8 h. The BET measurements and adsorption-desorption isotherms were performed at 77 K using Beckman Coulter SA 3100 Surface Area.

Solid State Nuclear Magnetic Resonance Spectroscopy. The ^{19}F Hahn echo Magic Angle Spinning (MAS) NMR spectra were acquired on an Avance 750 Bruker spectrometer (B_0 = 17.6 T), using a 2.5 mm ^{19}F optimized CP MAS probe, operating at a Larmor frequency of 705.8 MHz. The 90° pulse durations were set to 2.05 µs (ν_{RF} = 122 kHz) with an interpulse delay equal to one rotor period and recycle delays equal to 10 s. The ^{19}F chemical shifts were referenced to $CFCl_3$ at 0 ppm.

The ^{27}Al (I = 5/2) MAS and multiple-quantum MAS (MQMAS) NMR spectra were recorded on Avance III 750 and 850 Bruker spectrometers operating at B_0 = 17.6 T and 20.0 T (^{27}Al Larmor frequencies of 195.5 and 221.5 MHz, respectively). MAS spinning frequencies in the range 30 to 33 kHz were used. ^{27}Al 1D MAS spectra were recorded using a small pulse flip angle of 15° (0.55 µs at 17.6 T and 0.7 µs at 20.0 T) to ensure quantitative excitation of the whole spin system. The best ^{19}F decoupling efficiency was obtained using the PISSARO[34] decoupling (**Figure S5**) at RF fields of 80 kHz at 17.6 T and 104 kHz at 20 T. The recycle delay was set to 1

s. The two-dimensional (2D) z-filtered ^{27}Al MQMAS[35,36] spectra were recorded using RF-field strengths of ~80 kHz for triple-quantum (3Q) excitation and reconversion. The z-filter duration was set to one rotor period and the length of the central transition 90° selective pulse was 16 µs at 17.6 T and 8 µs at 20.0 T. 128 t_1 increments corresponding to one rotor period with 240 transients each were collected using the STATES procedure[37] and recycle delay ranging from 1 s to 3 s. ^{27}Al spectra were referenced to 1 M aqueous solution of $Al(NO_3)_3$. All spectra were simulated using the DMFIT software.[38]

Density Functional Theory (DFT) computations with periodic boundary conditions were conducted on structural models to benchmark the ^{27}Al and ^{19}F NMR parameters of $AlF_6(OH)_{6-x}$ and $FAl_2F_{10-z}(OH)_z$ local environments. Models consisting of 2x1x1 supercells of the β-AlF_3 unit cell with chemical compositions $AlF_2(OH)$ and $AlF_{1.875}(OH)_{1.125}$ were considered (cell parameters (Å): *a* = 13.862, *b* = 12.002 and *c* = 7.134). 16 structures with distributions of OH groups on the F1 and F2 sites ($AlF_2(OH)$) and 8 structures with distributions of OH groups on all F sites ($AlF_{1.875}(OH)_{1.125}$) were randomly generated using the supercell code.[39] For these 24 models, atomic positions were optimized by DFT keeping cell parameters fixed. The chemical shielding of ^{19}F and ^{27}Al and quadrupolar coupling NMR parameters of ^{27}Al were computed using the GIPAW[40] and PAW[41] methods, respectively. All DFT computations were performed with the Castep code,[42,43] using the PBE functional[44] and ultrasoft pseudopotential[45] generated "on-the-fly" as described in previous works.[46,47] A plane wave basis set energy cut-off of 600 eV and a Monkhorst-Pack grid density equal to 0.04 $Å^{-1}$ were used. ^{19}F calculated isotropic shieldings were converted to calculated isotropic chemical shifts using a relationship previously established (δ_{iso} (ppm) = -0.795 σ_{iso} + 89)[46,48] with the same computational parameters. ^{27}Al calculated isotropic shieldings were converted to calculated isotropic chemical shifts using

calculated and experimental[49] values for β-AlF_3 as secondary reference with the relation δ_{iso} (ppm) = - σ_{iso} + 548.2.

Hydrogen sorption measurements. Measurements were done using an automatic Sievert-type volumetric apparatus (HERA Hydrogen Storage System). The sample was first outgassed under primary vacuum over the night. The sample was then cooled under liquid nitrogen down to 77 K. The isotherm was then performed up to 50 bars. At each studied pressure, the equilibrium was assumed to be reached when the pressure difference is lower than 2kPa for 2 minutes. Then, the system was saturated under 70 bars. To desorb H_2, the sample was first heated to room temperature and then to 150°C (each step lasted 90 minutes) under vacuum. Then, a new absorption experiment was performed.

Results and discussion

Synthesis and characterizations of β-$AlF_{3-x}(OH)_x$ with high SSA.

β-$AlF_{3-x}(OH)_x$ was synthesized via microwave-assisted solvothermal method using aluminium nitrate ($Al(NO_3)_3 \cdot 9H_2O$) as aluminium precursor, aqueous hydrofluoric acid (HF_{aq}, 40%) as fluorinated agent with a molar ratio F/Al = 3 and an alcohol solvent. The mixtures were heated by MW according to the temperature profile shown in **Figure S2a**. A statistical DoE was applied to determine the influence of eight factors on the SSA: heating rate (Δt_1), plateau temperature (T_{syn}), plateau duration (Δt_{syn}), stirring speed, aluminium concentration ($[Al^{3+}]$), water proportion in the solvent, solvent nature (^{i}PrOH or EtOH) and drying method (classical oven or MW). Details are given as SI (**Table S1**). The data treatment, visualized from a Pareto chart, indicated that the nature of the solvent has the strongest impact on the SSA, followed by the plateau temperature in a lesser extent. Concerning this last parameter, for two experiments performed in the same conditions, the sample prepared at 130 °C systematically exhibited the highest SSA in

comparison with the sample prepared at 150 °C. It should be noted that a temperature below 130 °C does not allow the aluminium precursor dissolution. Concerning the solvent effect, microwave absorption depends on solvent properties which influence the size of the nanoparticles (**Figure S2b**).[50] Indeed, it has been shown that a low dielectric constant is correlated with the acceleration of the gelation process and then, an increased SSA.[51] Consequently, five different solvents, ^{i}PrOH, ^{i}PrOH/EtOH (1:1), EtOH, EtOH/MeOH (1:1) and MeOH, were used for the preparation of β-$AlF_{3-x}(OH)_x$ nanoparticles.

For each solvent, the SSA was determined by nitrogen sorption and calculated using the BET (Brunauer-Emmet-Teller) method (denoted as S_{BET} in the following). The average particle diameter, D_{BET}, was estimated by using the formula: $D_{BET} = {}^{6000}/_{(\rho . S_{BET})}$ with ρ the density of AlF_3 (2.678 g.cm^{-3}). In the following, the samples are denoted by their S_{BET} value which is the determining factor in this work. N_2 sorption results illustrate the correlation between the decrease of the boiling point of the solvent (**Table S3**) and the decrease of the particle size as well as the increase of S_{BET} (**Table 1**). The difference in S_{BET} values of S-300 and S-345, despite similar particle diameters (7 and 6 nm, respectively), can be explained by different porosities. Indeed, the pore volumes are 0.3 and 0.6 cm^3.g^{-1} for S-300 and S-345, respectively, the later allows presuming some capacity of adsorption, discussed below.

For the five samples, three different kinds of nitrogen adsorption-desorption isotherms[52] are observed (**Figure 2**). The type II isotherm appears for samples with the lowest S_{BET} (S-25 and S-60). For both materials, a pseudo-saturation plateau is reached for a high relative pressure. This kind of isotherms is obtained for non-porous or macroporous materials. For intermediate S_{BET} (S-185 and S-300), the type II isotherm without pseudo-saturation plateau is observed with H_3 hysteresis loop. It is assumed that the observed mesoporous behaviour is assimilated to

intergranular mesoporosity of non-rigid aggregates. For the sample with the highest S_{BET} (S-345), type IV isotherm characteristic of mesoporous solid is observed and H_{2b} hysteresis loop is visible. The sample is constituted of agglomerates in which the particles are slightly connected inducing interconnected mesopores. This feature explains why, despite similar particle sizes, S_{BET} of S-345 is significantly higher than that of S-300.

Despite the low crystallinity of samples with high SSA, good fits of experimental data are obtained from Rietveld refinements (**Table S2**), confirming the phase purity (**Figure 3** and Rietveld refinement **Figure S3**). For samples with larger SSA, an increasing preferred orientation effect along the (002) plane is observed together with the decrease of particle sizes related to the crystal growth limitation along tunnels of HTB structure. The PXRD patterns exhibit a line broadening correlated with the small size of the crystallite (*i.e.* the size of the coherent diffraction domains <L>). The calculated particle diameters, $D_{XRD} = 4/3 \times <L>$, are reported in **Table 1**.

The morphology of the β-$AlF_{3-x}(OH)_x$ samples was investigated by TEM (**Figure 4**). Surprisingly, the morphology of the samples consists of hollow spherules for which walls are built up from spherical isolated nanoparticles were observed expected for S-345. The average particle diameters (D_{TEM}) are gathered in **Table 1**. A relative agreement is found between diameters of particles evaluated from BET, XRD and TEM experiment except for S-25 which can be explain by multidomains particles.

This structure is similar to the one observed in Pickering emulsions (oil dispersed in water). During such a mechanism, the water/oil interface is stabilized by silica nanoparticles.[53] In our study, it can be assumed that microwave-assisted synthesis in autoclave leads to the formation of gas bubbles in the reaction media. These gas bubbles can be assimilated to a foam where the

liquid/gas interface is stabilized by β-$AlF_{3-x}(OH)_x$ particles. In this respect, the germination arises at the liquid/gas interface until it is totally covered by nanoparticles leading to the formation of hollow nanostructures (**Figure 5**).

According to this mechanism, it is expected that the size of the gas bubbles controls the size of hollows spherules as well as the wall thickness are given in **Table 1**. When the boiling point of the solvent is high (*eg*. 82°C for S-25), the autogenous pressure in the MW reactor is low (4.7 bar) and the gas bubbles grow up leading to large hollow spherules with a rigid structure. Solvents with lower boiling points (**Table 1**) lead to higher pressures (5.2 bar for S-60, 5.5 bar for S-185, 7.0 bar for S-300) and consequently smaller bubbles and narrower structures. These smaller bubbles lead to higher surface available for germination and the crystal growth is prevented due to constant matter quantity. S-345 constitutes an exception because agglomerates of nanoparticles are mainly observed. Few hollow spherules appeared (**Figure S4**) but they are not representative of the sample. It is worth to notice a powdery aspect except for S-345 which is composed of translucent blocks (**Figure 6**). Crystallized domains observed for S-345 on high resolution TEM images (**Figure 7**a) and the corresponding selected area electron diffraction pattern shows inter-reticular distances of 6.1 Å and 3.58 Å characteristic for (110) and (111) β-AlF_3 reticular planes, respectively (**Figure 7**b-c).

Chemical compositions from TGA

The thermal behaviour was investigated to determine the formulation and the thermal stability of the *β*-$AlF_{3-x}(OH)_x \cdot nH_2O$ samples (**Figure 8**). Under N_2, the TGA shows three weight losses.[54] The first one occurs between room temperature and 200 °C and corresponds to the loss of weakly adsorbed water (reaction (1)). Despite storage in a glovebox, water molecules are adsorbed by the sample during the preparation. The second weight loss between 200 and 500°C is assigned to

the dehydroxylation of β-$AlF_{3-x}(OH)_x$ (reaction (2)) and allows to estimate the hydroxyl content for each sample. Finally, above 500 °C the oxyfluorides $AlF_{3-x}O_{x/2}$ react with the little amount of water (less than 3 ppm) contained in the N_2 atmosphere and are transformed very slowly into aluminium oxide Al_2O_3 (reaction (3)).

Dehydration (RT - 200°C): β-$AlF_{3-x}(OH)_x \cdot nH_2O \rightarrow \beta$-$AlF_{3-x}(OH)_x + n\ H_2O$ (1)

Dehydroxylation (200°C - 500°C): β-$AlF_{3-x}(OH)_x \rightarrow AlF_{3-x}O_{x/2} + x/2\ H_2O$ (2)

Pyrohydrolysis (> 500°C): $AlF_{3-x}O_{x/2} + (3-x)/2\ H_2O \rightarrow ½\ Al_2O_3 + (3-x)\ HF$ (3)

The formulations (i.e. x and n values in the β-$AlF_{3-x}(OH)_x \cdot nH_2O$ formula) have been deduced from weight loss values: x = 0.55 and n = 0.25 for S-25, x = 0.56 and n = 0.18 for S-60, x = 0.52 and n = 0.25 for S-185, x = 0.59 and n = 0.30 for S-300 and x = 0.61 and n = 0.49 for S-345. The values of x will be better determined from the high-field solid state NMR study presented in the next part.

Solid state NMR spectroscopy

^{27}Al solid state NMR spectroscopy of nanostructured β-$AlF_{3-x}(OH)_x$

^{27}Al high-field solid state NMR has been previously used to probe and quantify the various $AlF_{6-y}(OH)_y$ (or $AlF_{6-y}(OH_2)_y$) environments in β-$AlF_{3-x}(OH)_x \cdot nH_2O$ (x = 0.4 and 0.6),[26] pyrochlore $AlF_{1.8}(OH)_{1.2} \cdot 0.3H_2O$,[27] annealed β-$AlF_{2.6}(OH)_{0.4}$,[54] $Al_{0.82}\square_{0.18}F_{2.46}(H_2O)_{0.54}$,[55] and pyrochlore $AlF_{1.4-1.9}(OH)_{1.6-1.1} \cdot H_2O$.[56] The ^{27}Al NMR features of these environments have been established experimentally (**Table S4**), showing that larger amounts of OH substituting F atoms in the Al first coordination sphere (y value) leads to higher ^{27}Al isotropic chemical shift (δ_{iso}) values. This trend was confirmed here by DFT computations with periodic boundary conditions of the ^{27}Al NMR parameters using the GIPAW method.[40] For that purpose, structural models consisting of a 2x1x1 supercell of the β-AlF_3 unit cell with chemical compositions $AlF_2(OH)$ and

$AlF_{1.875}(OH)_{1.125}$ have been considered to benchmark a variety of $AlF_{6-y}(OH)_y$ environments. They were randomly selected amongst all possible configurations considering either a distribution of OH groups in all F sites ($AlF_2(OH)$), or a distribution of OH groups only in the F1 and F2 sites ($AlF_{1.875}(OH)_{1.125}$) of the 2x1x1 supercell. In all cases, results of the DFT-GIPAW computations indicate an increase of the ^{27}Al isotropic chemical shift of about 4 to 5 ppm when substituting one F atom by one OH group in the Al first coordination sphere, i.e. increasing y by one unit (**Figure 9**). Details about these calculations are given as SI (**Table S5**).

In that respect, ^{27}Al NMR could provide an alternative way to quantitatively estimate the amount of hydroxyl groups in an aluminium hydroxyfluoride and to refine its chemical formula (the amount of adsorbed water cannot be estimated by this way and consequently all formulations do not include nH_2O). To be efficient, this method requires high-resolution ^{27}Al solid-state NMR spectra allowing distinguishing the signatures of each $AlF_{6-y}(OH)_y$ environment. ^{27}Al is a 5/2-spin nucleus subjected to quadrupolar interaction. In that case, use of high magnetic fields allows to greatly enhance the resolution in MAS spectra, since the chemical shift dispersion increases with the magnetic field while second-order quadrupolar broadenings scale down.[57] Moreover, the remaining second order quadupolar broadening at high field can be efficiently removed by the MQMAS NMR technique which allows obtaining a 2D spectrum with a truly high-resolution isotropic dimension from which the isotropic chemical shift and quadrupolar coupling constant of each ^{27}Al resonance can be accurately determined.[35,36] The quantitative ^{27}Al MAS spectra of the five β-$AlF_{3-x}(OH)_x \cdot nH_2O$ samples have then been recorded at high magnetic fields of 17.6 and 20.0 T (**Figure 10**, **Figure 11** and **Figure S8**). They show strong similarities with those previously obtained at 17.6 T for nanostructured β-$AlF_{3-x}(OH)_x$ materials.[26] For all samples, the central transition region of the MAS spectrum exhibits a main

peak at -15 ppm flanked by several shoulders at higher chemical shift values and a slight broadening of the ^{27}Al resonances is observed when S_{BET} of the sample increases. 2D MQMAS experiments also performed at high fields clearly provide enhanced spectral resolution and allow evidencing four distinct ^{27}Al resonances for sample S-185: a relatively narrow one peaking at about -15 ppm, two broader peaks with ^{27}Al isotropic chemical shifts of -11 and -8.5 ppm and a fourth broader line of weaker intensity located at about -5 ppm. These 2D MQMAS spectra also reveal lineshapes characteristic of a distribution of the quadupolar interaction for the three broader contributions, consistent with the analysis of the ^{27}Al satellite transition spinning sideband manifolds in MAS spectra.

Simulations of both 2D MQMAS and quantitative 1D MAS spectra of S-185 were thus done considering Gaussian distributions of δ_{iso} (isotropic chemical shift) and C_Q (nuclear quadrupole coupling constant) values for each of the four individual resonance. Considering the disorder induced by the partial occupation of the F sites by OH groups and the nanostructuration of the samples, this leads to more realistic line shapes and better reconstructions, compared to the previous solid state NMR study of nanostructured β-$AlF_{3-x}(OH)_x$[26] with deconvolutions of the ^{27}Al 1D MAS spectra achieved with three Gaussian lines. The MQMAS spectra of S-185 were first simulated in order to obtain primary sets of parameters. Since MQMAS experiments can lead to slightly underestimated average C_Q values the 1D ^{27}Al MAS spectra were reconstructed by refining the quadrupolar coupling distribution parameters and the amplitude of each resonance while keeping the isotropic chemical shift distribution fixed to the value issued from the simulation of the MQMAS spectra. The relative intensities of the resonances were calculated from line shape integrations of the central transitions. Satisfactory fits of the MAS spectra of the four other samples have been achieved with similar parameters (**Figure 11**, **Table 2**), the width

of the chemical shift distribution being the only value to vary significantly, accounting for the observed slight broadening of the ^{27}Al MAS spectra when the S_{BET} of the sample increases.

Following the DFT-GIPAW computations for benchmark $AlF_{6-y}(OH)_y$ environments indicating a 4 to 5 ppm increase of the ^{27}Al isotropic chemical shift as y increases by one unit (**Figure 9**) and in agreement with previous works[25,27,54–56] (**Table S4**), these four resonances at about -15, -11, -8 and -5 ppm can be unambiguously assigned to AlF_6, $AlF_5(OH)$, $AlF_4(OH)_2$ and $AlF_3(OH)_3$ units, respectively. Although DFT computations lead to slightly overestimated average ^{27}Al C_Q values for the considered static 2x1x1 supercell models (**Figure S6**), it also supports this assignment. Indeed, it shows an increase of both the mean value and the width of the calculated C_Q distribution associated to the distinct $AlF_6(OH)_y$ environments as y increases, nicely mimicking the observed experimental trends.

On this basis, one observes that the relative intensity of the AlF_6 resonance is smaller (and that of the $AlF_3(OH)_3$ resonance is larger) for the samples with large S_{BET}. Each individual resonance being assigned to a single environment, the global compositions deduced from their relative intensities appear to be improved with respect to previous work.[26] The calculated compositions can be compared to those of the dehydrated phases determined by TGA (also reported in **Table 2**) since the amount of adsorbed water cannot be determined by ^{27}Al NMR. Except for S-60, the differences between x values are small (less than 8%) showing the effectiveness of ^{27}Al NMR for estimating the hydroxide content in aluminium hydroxyfluorides. It shows here that the hydroxide content in the β-$AlF_{3-x}(OH)_x$ samples with S_{BET} ranging from 25 to 185 $m^2.g^{-1}$ is almost independent of the S_{BET} value, while it is slightly higher for the two samples with the largest S_{BET} (300 and 345 $m^2.g^{-1}$). One should also point out that, in all cases, the distributions of $AlF_{6-y}(OH)_y$ units determined by ^{27}Al high-field NMR are relatively close to those calculated

assuming a random distribution of OH groups, either in only the F1 and F2 sites,[26] or in all F sites of the β-AlF_3 structure (**Table 3**).

^{19}F solid state NMR spectroscopy of nanostructured β-$AlF_{3-x}(OH)_x$

Due to similar environments of the four distinct F sites in the structure of β-AlF_3 (**Table S7**), the ^{19}F NMR resonances are not resolved in the ^{19}F MAS NMR spectra recorded by Chupas *et al*.[49] More scattered ^{19}F δ_{iso} values are expected in β-$AlF_{3-x}(OH)_x$ samples since the ^{19}F δ_{iso} value of a fluorine atom at the vertex of an $AlF_{6-y}O_y$ octahedron increases with the oxygen content (y).[56,58] Nevertheless, although recorded at high fields, the ^{19}F MAS NMR spectra (**Figure 12**) remain poorly resolved, suggesting the presence of several overlapping ^{19}F resonances with broad chemical shift distributions related to large distributions of interatomic distances around each types of fluorine environments.

In the HTB structure, each fluoride anion bridges two AlX_6 (X = F, OH) octahedra and can be associated to distinct types of $FAl_2F_{10-z}(OH)_z$ dimer of octahedra. For the studied compositional range, only six $FAl_2F_{10-z}(OH)_z$ groups have significant probabilities of occurrence (z = 0 to 5) (**Table 4**) considering a random distribution of OH groups either in only F1 and F2 sites or in all F sites of the structure. GIPAW-DFT computations of the ^{19}F isotropic chemical shifts performed for the considered 2x1x1 $AlF_2(OH)$ supercell models indicate a strong overlap of the chemical ranges associated to distinct $FAl_2F_{10-z}(OH)_z$ groups and an increase of the average ^{19}F chemical shift of about 3 ppm is observed when increasing z by one unit (**Figure S7 and Table S6**).

Reconstructions of the ^{19}F MAS spectra were thus achieved using six distinct resonances (**Table 5** and **Figure S9**) which were assigned according to both DFT-GIPAW computations and the reported ^{19}F chemical shift trends in hydroxy/oxyfluorides of aluminium.[48,49] The position of each line was kept similar whatever the sample. In line with ^{27}Al NMR results, the relative

amount of F-$Al_2F_{10-z}(OH)_z$ units with high z values increases for the sample with the largest amount of OH groups, i.e. showing the largest S_{BET} values. And as for the distributions of $AlF_{6-y}(OH)_y$ units determined by ^{27}Al solid-state NMR, for all samples, the distributions of F-$Al_2F_{10-z}(OH)_z$ groups determined by ^{19}F solid-state NMR (**Table 5**) are close to those expected assuming a random distribution of OH groups either only in F1 and F2 sites[26] or in all F sites of the β-AlF3 structure (**Table 4**).

Hydrogen adsorption properties of nanostructured β-$AlF_{3-x}(OH)_x$ samples

Given its large SSA combined to an intergranular mesoporosity, S-345 was tested as solid-state hydrogen storage material, along with S-60 and S-185 for comparison. For each sample, hydrogen adsorption was measured and five cycles were performed at 77 K (C1 to C5); the sixth one was performed at room temperature. The hydrogen adsorption isotherms of S-345 and the hydrogen sorption values as a function of SSA are represented on **Figure 13**. The initial adsorption capacities increase with the SSA and that of S-345 reaches 1.45 wt. %, comparable to activated carbon or some MOFs[59] demonstrating the ability of high SSA β-$AlF_{3-x}(OH)_x$ to store H_2. Nevertheless, whatever the sample, the weight capacity drops by a factor of ~2 between the first and the second cycle and remains almost constant thereafter, while the adsorption tests have no influence on the SSA values and PXRD patterns. Complementary experiments are required to understand this drop of capacity. The adsorption capacities at room temperature, significantly lower, less than 0.1 wt. % for S-345 (C6 curve on **Figure 13 a**), demonstrates that the Van der Waals interactions between the host and hydrogen are weak. According to the method described by Myers,[60] the value of the hydrogen enthalpy of binding energy for S-345 is calculated close to ~5 $kJ.mol^{-1}$ (determined from the adsorption isotherms recorded at 4 different temperatures 77, 87, 107 and 125 K) is in agreement with low capacity storage at RT owing to the optimal values

should be in the range 20-40 kJ.mol^{-1}.[61,62] The non-negligible hydroxyl rate could play a role in this low value of the binding energy.

Conclusion

Nanostructured β-$AlF_{3-x}(OH)_x$ materials were successfully prepared by microwave-assisted solvothermal synthesis. Optimised synthesis allow obtaining nanoparticles with diameter ranging from 80 to 7-10 nm and related specific surface area (S_{BET}) ranging from 25 to 345 m².g^{-1}. The OH contents of these β-$AlF_{3-x}(OH)_x$ materials, estimated using ^{27}Al high-field solid-state NMR, increase slightly, from ~16% ($AlF_{2.52}(OH)_{0.48}$) to ~ 19% ($AlF_{2.42}(OH)_{0.58}$). ^{27}Al high-field NMR spectra allow to discriminate four resonances assigned to four distinct $AlF_{6-y}(OH)_y$ groups (y = 0 to 3) on the basis of DFT computations with periodic boundary conditions of the ^{27}Al NMR parameters. The synthesis strategy allows tuning the morphology of β-$AlF_{3-x}(OH)_x$ nanomaterials, either by forming hollow nanostructures or isolated nanoparticles. The hollow spherule formation is assumed to be driven by to a Pickering emulsion mechanism in which gas bubbles can be assimilated to a foam where the liquid/gas interface is stabilized by β-$AlF_{3-x}(OH)_x$ particles.

Preliminary results of hydrogen adsorption for the β-$AlF_{3-x}(OH)_x$ sample with the highest S_{BET} (345 m^2.g^{-1}) and an appealing cumulative pore volume of 0.060 cm^3.g^{-1} proves the ability of nanofluorides for gas storage applications. Further experiments are on-going to enhance the adsorption energy by increasing the fluoride content through gas-phase fluorination of the tested materials.

ASSOCIATED CONTENT

Supporting Information. The following files are available free of charge on the ACS Publications website at DOI: Allotropic structures of AlF_3, DoE method, dielectric properties and boiling point of the different solvents, Rietveld refinements, microscope images and solid-state NMR data: ^{19}F decoupling, bibliographic data, ^{27}Al isotropic chemical shift ranges and quadrupolar coupling constants of the various $AlF_{6-y}(OH)_y$ species and ^{19}F isotropic chemical shift ranges of the various $FAl_2F_{10-z}(OH)_z$ species calculated using the DFT-GIPAW method for 2x1x1 supercell structural models, ^{27}Al MAS NMR spectra, structural data on β-AlF_3, ^{19}F MAS experimental and reconstructed spectra (PDF) and cif files of the 24 supercell structural models (ZIP).

ACKNOWLEDGMENT

The authors are indebted to Le Mans Université (V. Camus-Génot) for doctoral grants and the Région des Pays de la Loire (J. Lhoste, Gis-Perle project). Thanks are also due to the Université Bretagne Loire, University of Le Mans and to ANR Programme National de Recherche – OPIFCAT for the postdoctoral grant of R. Moury. The authors gratefully acknowledge the "X-ray Diffusion and Diffraction" and the "Electron Microscopy" technical platforms of IMMM (Le Mans University). Financial support from the TGIR-RMN-THC FR3050 CNRS for conducting the solid-state NMR experiments is gratefully acknowledged. DFT computations have been performed at the “Centre de Calcul Scientifique en Région Centre” facility (CCRS, Orléans, France) under the CASCIMODOT program. The authors also thank Alain Jouanneaux (IMMM) for help for the DoE.

AUTHOR INFORMATION

Corresponding Authors

*JL: e-mail: jerome.lhoste@univ-lemans.fr;

*CL: e-mail: christophe.legein@univ-lemans.fr

Present Address.

† Institut Néel, CNRS/UGA UPR 2940, Pôle Optique et Microscopies. 25, Rue des Martyrs - BP 166, 38042 Grenoble Cedex 9, France

Author Contributions

The manuscript was written through contributions of all authors. All authors have given approval to the final version of the manuscript.

ORCID

Jean-Louis Bobet : 0000-0001-7838-7004

Monique Body: 0000-0002-5895-3731

Valentine Camus-Génot: 0000-0003-2885-2689

Franck Fayon: 0000-0001-5086-5625

Amandine Guiet: 0000-0001-7590-1119

Stéphanie Kodjikian: 0000-0001-7304-3675

Romain Moury: 0000-0002-1198-2586

Marc Leblanc: 0000-0001-7958-0359

Christophe Legein: 0000-0001-7426-8817

Jérôme Lhoste: 0000-0002-4570-6459

Vincent Maisonneuve: 0000-0003-0570-953X

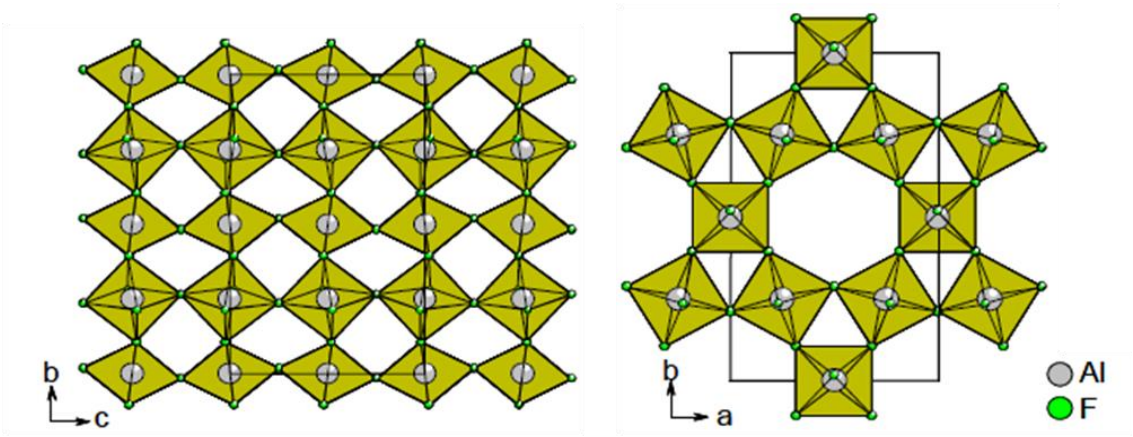

Figure 1. [100] (left) and [001] (right) projection of the structure of β-AlF_3.

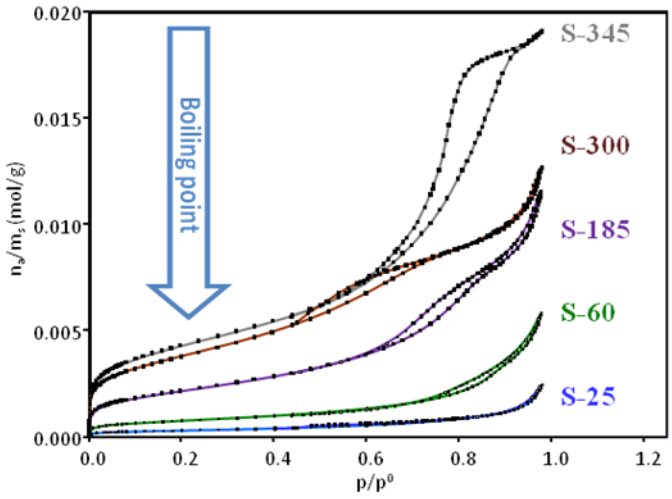

Figure 2. Nitrogen adsorption-desorption isotherms at 77 K for the β-$AlF_{3-x}(OH)_x$ samples.

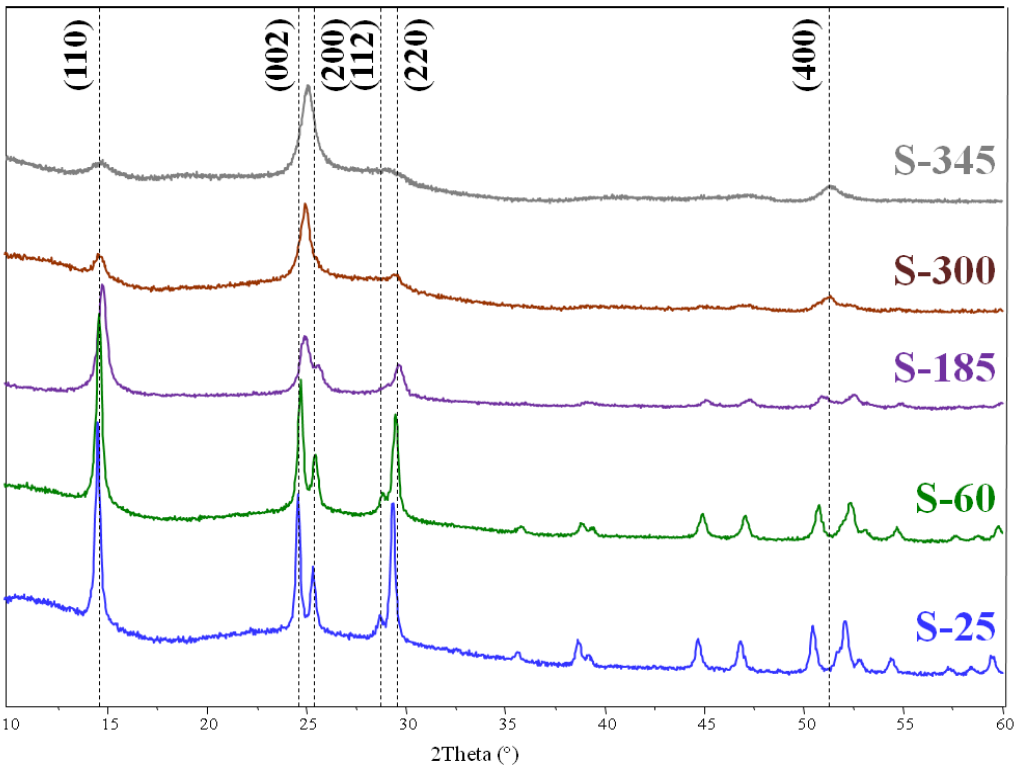

Figure 3. PXRD patterns of the β-$AlF_{3-x}(OH)_x$ samples.

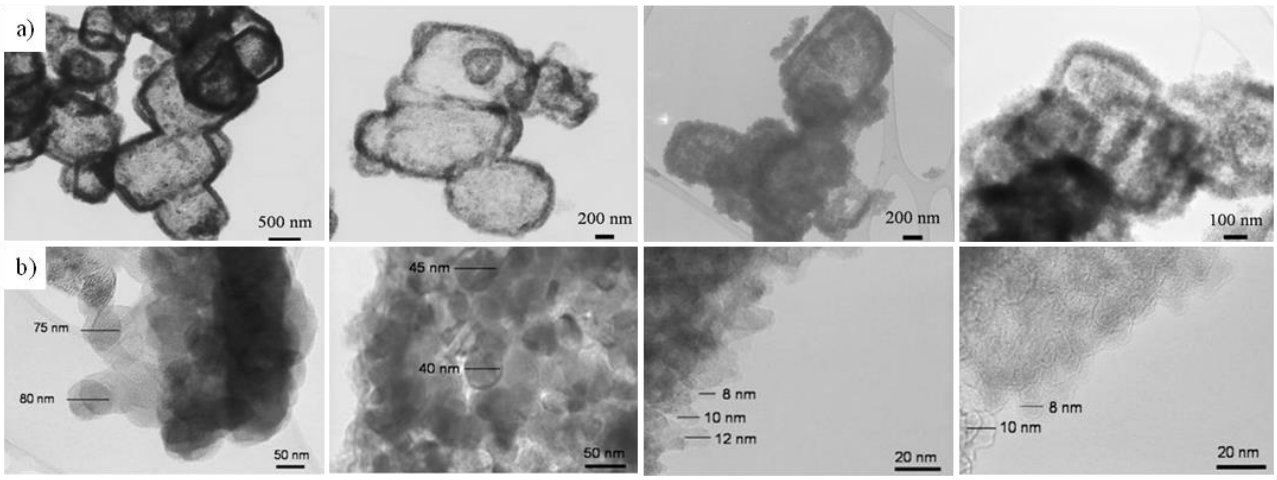

Figure 4. TEM images of a) hollow spherules and b) nanoparticles of (from left to right) S-25, S-60, S-185 and S-300.

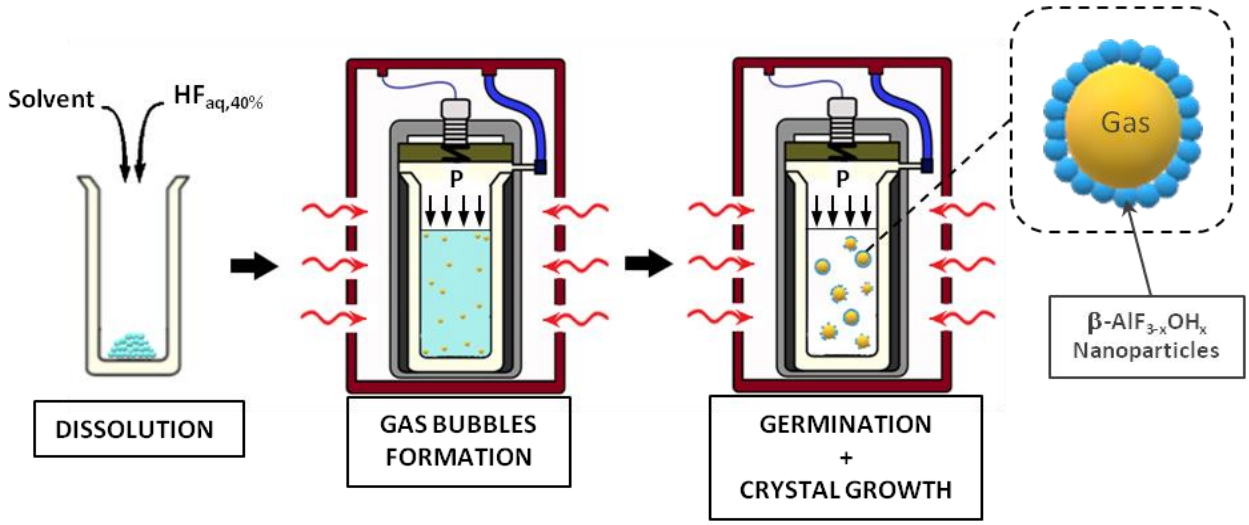

Figure 5. Scheme of proposed mechanism for hollow nanostructures formation.

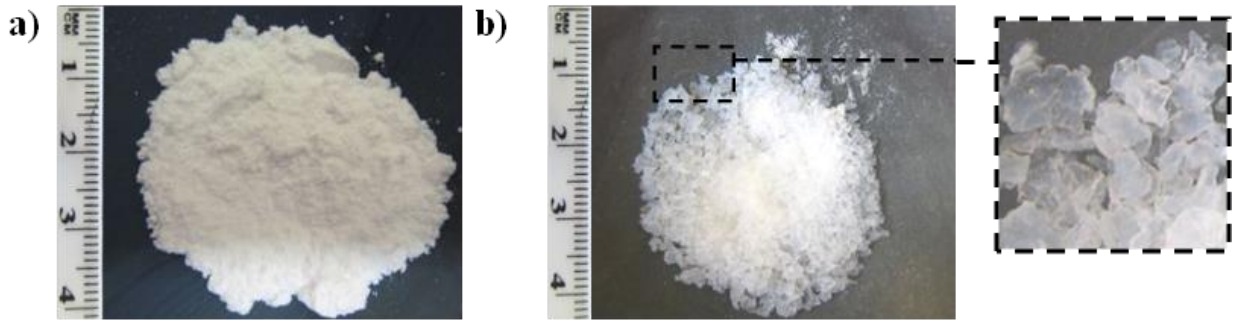

Figure 6. Pictures of a) S-25 and b) S-345 samples.

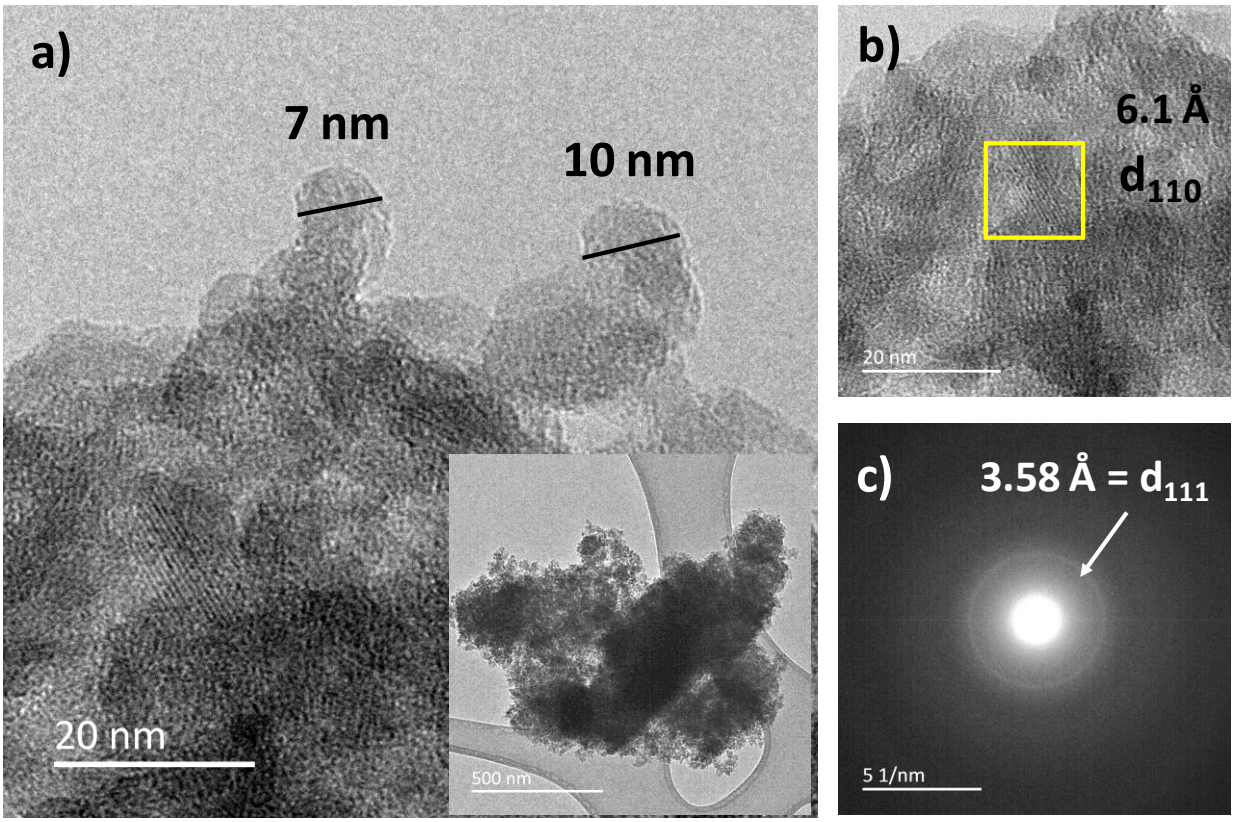

Figure 7. a) TEM images of S-345. b) High resolution TEM image of S-345. c) Corresponding selected area electron diffraction.

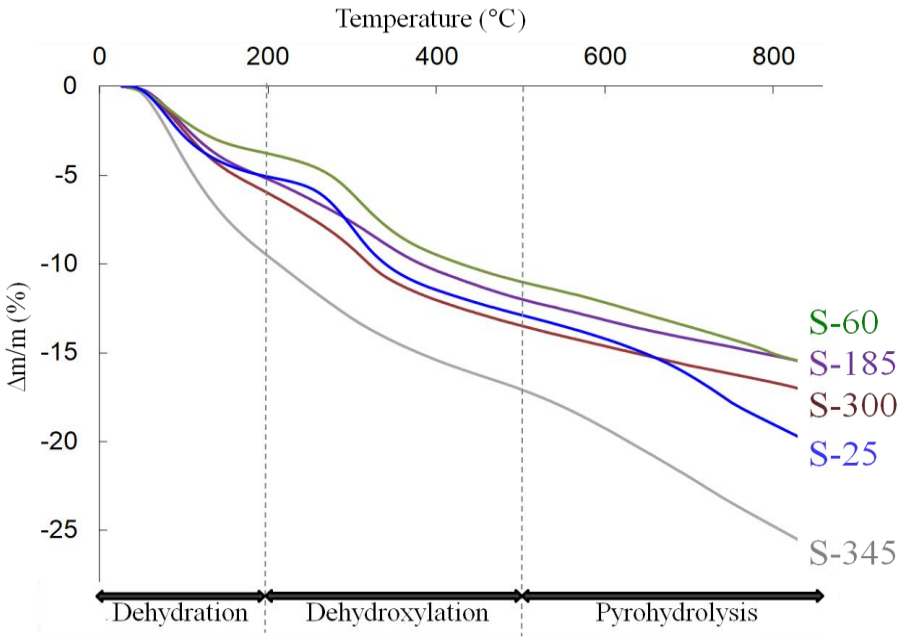

Figure 8. TGA of the β-$AlF_{3-x}(OH)_x$ samples under N_2.

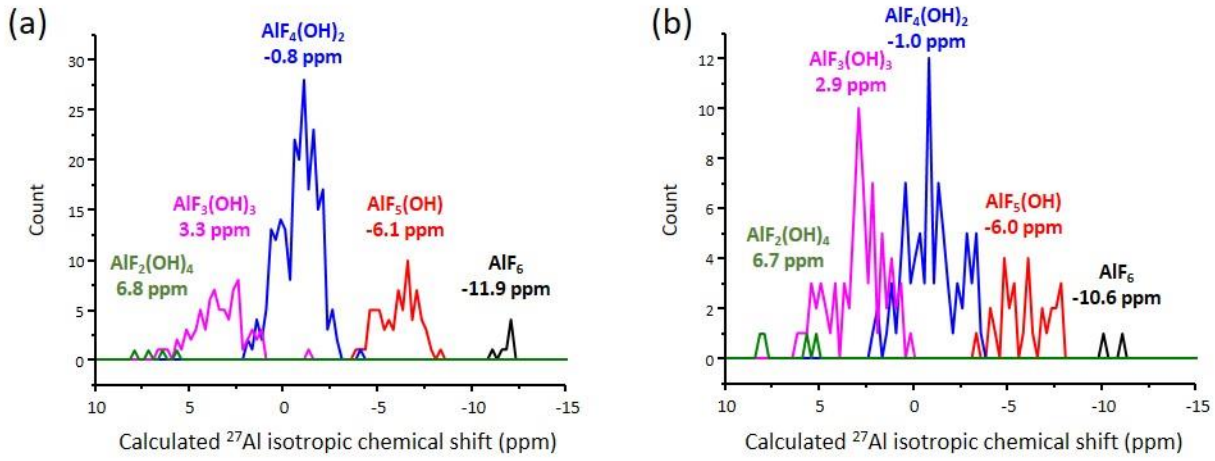

Figure 9. Histogram of the calculated ^{27}Al isotropic chemical shifts of all $AlF_{6-y}(OH)_y$ species found in the (a) 16 $AlF_2(OH)$ and (b) 8 $AlF_{1.875}(OH)_{1.125}$ supercell models, considering a distribution of OH group in (a) only F1 and F2 sites and (b) all F sites of the structure. The average values are indicated for each $AlF_{6-y}(OH)_y$ specie.

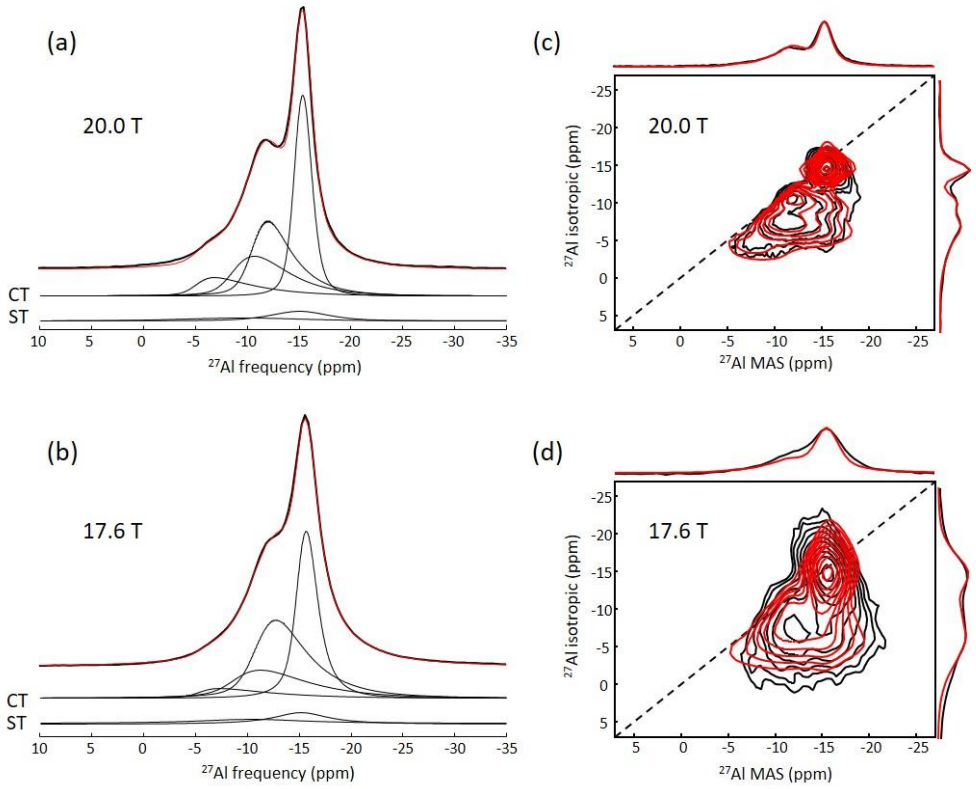

Figure 10. ^{27}Al quantitative MAS ((a) 30 kHz, (b) 33 kHz) spectra of S-185 (black) recorded at (a) 20.0 T and (b) 17.6 T and their reconstructions (red) with four individual resonances. The central transitions (CT) and zero-order satellite transition spinning sidebands (ST) are shown below the experimental spectra. ^{27}Al MQMAS ((c) 30 kHz, (d) 33 kHz) spectra (black) recorded at (c) 20.0 T and (d) 17.6 T and their reconstructions with the same parameters as those used in (a, b).

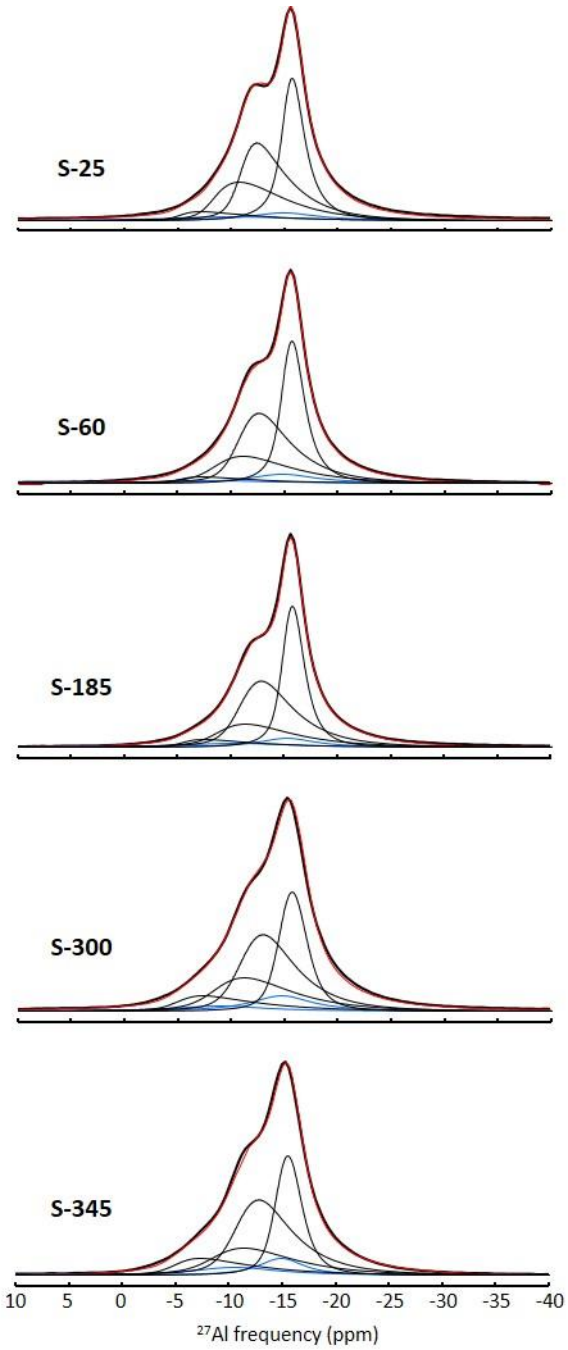

Figure 11. ^{27}Al quantitative MAS (33 kHz) spectra, recorded at 17.6 T, of the five samples S-25, S-60, S-185, S-300 and S-345. Reconstructions with four individual resonances are shown as red lines. The central transition (black) and zero-order satellite transition spinning sidebands (blue) of the four individual contributions are shown below the experimental spectra.

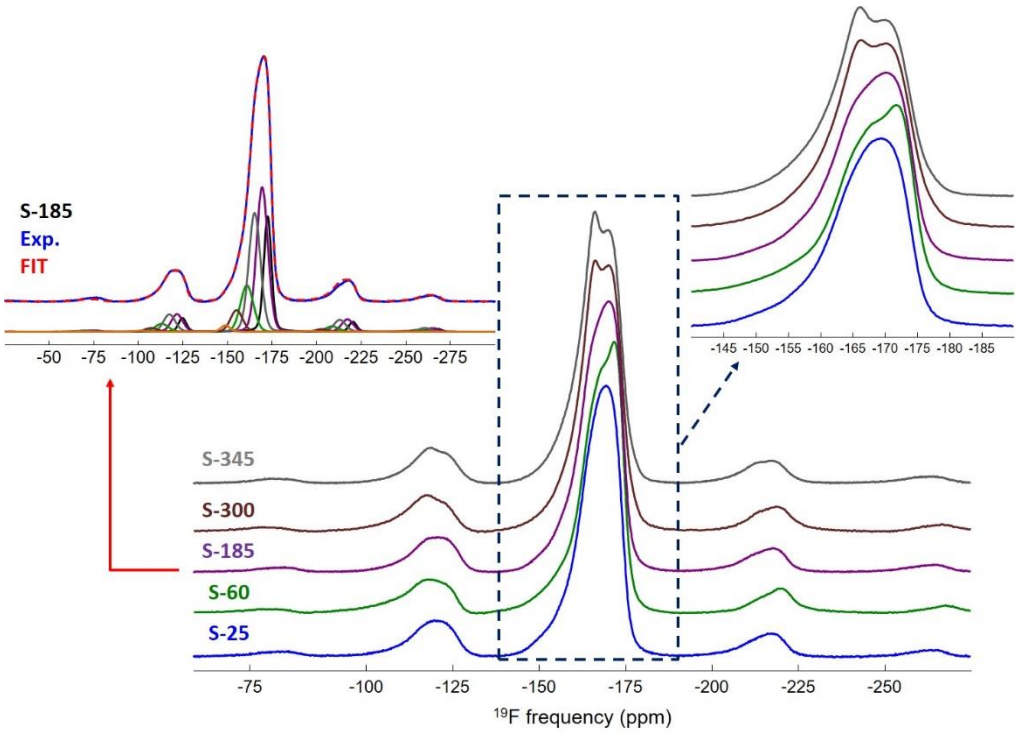

Figure 12. ^{19}F MAS (33 kHz) spectra recorded at 17.6 T of S-25, S-60, S-185, S-300 and S-345. Top right: enlargement of the isotropic lines. Top left: experimental (in blue) and reconstructed (red dashed line) spectra of S-185. The six individual resonances used for the fit are shown below.

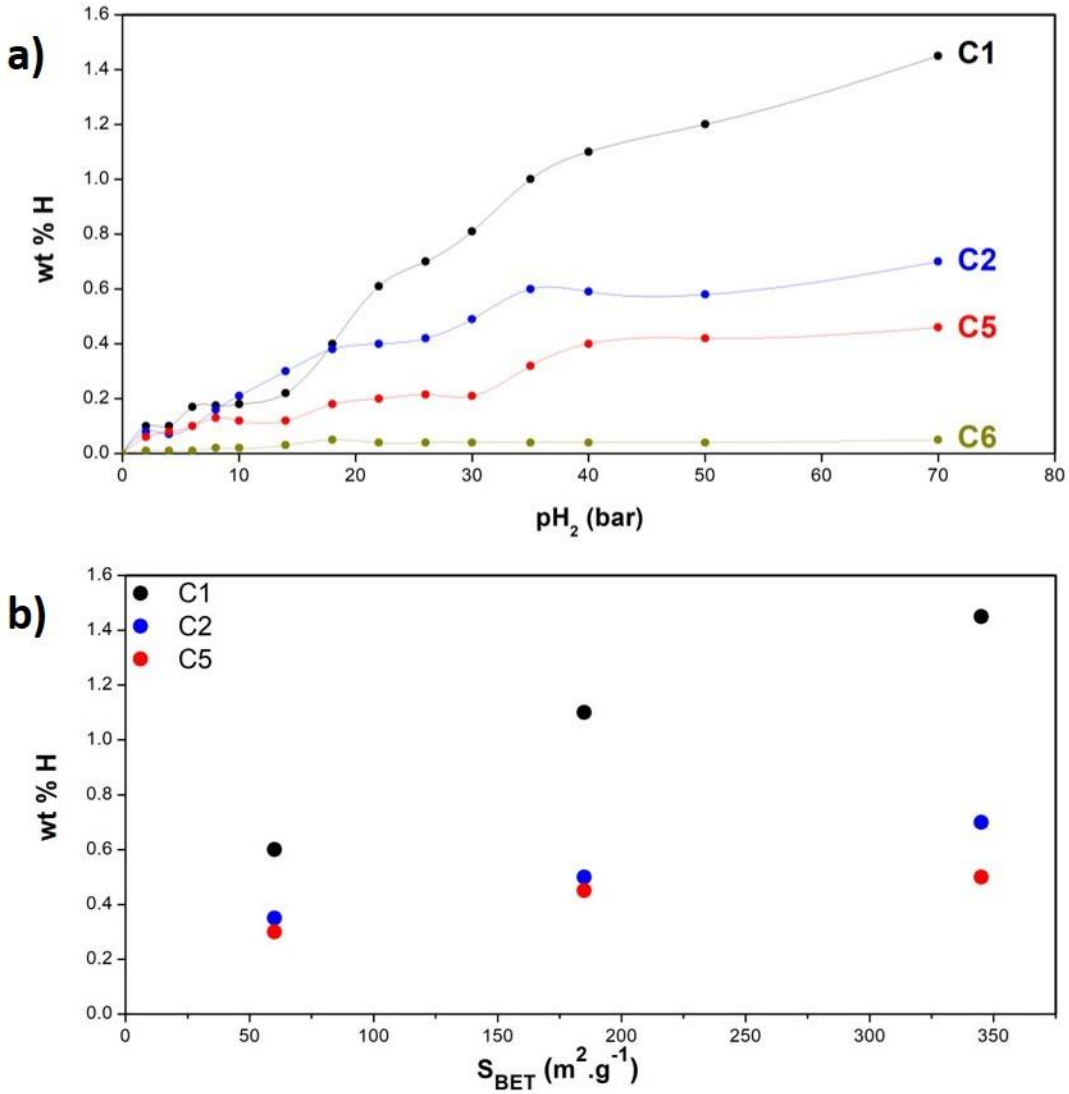

Figure 13. a) Absorption isotherms for the sample S-345. C1, C2, C5 and C6 represent the first, the second, the fifth and the sixth cycle, respectively. C1, C2 and C5 were performed at 77 K whereas C6 was performed at room temperature. **b)** Hydrogen sorption values vs specific surface area for C1 (in black), C2 (in blue) and C5 (in red).

Table 1. Solvothermal media used for the MW synthesis and their boiling points (°C) and corresponding S_{BET} ($m^2.g^{-1}$), pore volume ($cm^3.g^{-1}$), diameters (nm) estimated from BET measurements, D_{BET}, from Rietveld refinements, D_{DRX}, and from TEM analyses, D_{TEM}, wall thickness (nm) and hollow spherule size (nm) of the synthesized samples of β-$AlF_{3-x}(OH)_x$.

Sample	**Medium**	**Boiling point**	**S_{BET}**	**Pore volume**[(2)]	**D_{BET}**	**D_{DRX}**	**D_{TEM}**	**Wall**	**Hollow spherule**
S-25	^{i}PrOH	82.3	25	0.03	86	34	75-80	170	1400
S-60	^{i}PrOH/ EtOH (1:1)	80.5[(1)]	60	0.16	36	26	40-45	160	950
S-185	EtOH	78.3	185	0.28	12	15	8-12	110	950
S-300	EtOH/ MeOH (1:1)	72[(1)]	300	0.33	7	13	8-10	35	240
S-345	MeOH	64.7	345	0.60	6	9	7-10	-	-

[(1)] Calculated from Raoult and Antoine laws. [(2)] Total volume measured at $\frac{p}{p^0} = 0.99$.

Table 2. Mean (<δ_{iso}>) and width of the distribution (Δcs) of δ_{iso} values (ppm), mean (<C_Q>) and width of the distribution (ΔC_Q) of C_Q values (MHz), asymmetry parameter η_Q and relative line intensity I (%) deduced from the reconstruction of the ^{27}Al spectra of the five β-$AlF_{3-x}(OH)_x$ samples, assignment of the ^{27}Al NMR lines, chemical composition inferred from these assignments and (in italic) chemical composition inferred from TGA.

Sample	**<δ_{iso}> (±0.2)**	**Δcs (±0.2)**	**<C_Q> (±0.2)**	**ΔC_Q (±0.2)**	**η_Q (±0.1)**	***I* (±1)**	**Assignment**	**Composition**
S-25	-15.3	1.4	1.9	1.3	0.5	34.6	AlF_6	$AlF_{2.49}(OH)_{0.51}$
	-11.2	2.2	3.6	3.0	1	35.5	$AlF_5(OH)$	
	-8.2	2.2	4.7	3.0	1	23.8	$AlF_4(OH)_2$	*$AlF_{2.45}(OH)_{0.55}$*
	-5.3	2.0	5.5	4.3	0.5	6.2	$AlF_3(OH)_3$	
S-60	-15.2	1.5	1.9	1.3	0.5	35.6	AlF_6	$AlF_{2.52}(OH)_{0.48}$
	-11.2	3.0	3.6	3.0	1	37.7	$AlF_5(OH)$	
	-8.5	3.0	4.7	3.0	1	21.7	$AlF_4(OH)_2$	*$AlF_{2.44}(OH)_{0.56}$*
	-5.3	2.2	5.5	4.3	0.5	4.9	$AlF_3(OH)_3$	
S-185	-15.2	1.5	1.9	1.3	0.5	35.1	AlF_6	$AlF_{2.52}(OH)_{0.48}$
	-11.3	3.2	3.6	3.0	1	38.9	$AlF_5(OH)$	
	-8.7	3.0	4.7	3.0	1	19.8	$AlF_4(OH)_2$	*$AlF_{2.48}(OH)_{0.52}$*
	-5.5	2.2	5.5	4.3	0.5	6.2	$AlF_3(OH)_3$	
S-300	-15.2	2.2	1.9	1.3	0.5	28.9	AlF_6	$AlF_{2.43}(OH)_{0.57}$
	-11.4	3.5	3.6	3.0	1	37.4	$AlF_5(OH)$	
	-8.5	3.5	4.7	3.0	1	23.4	$AlF_4(OH)_2$	*$AlF_{2.41}(OH)_{0.59}$*
	-5.2	3.0	5.5	4.3	0.5	10.3	$AlF_3(OH)_3$	
S-345	-15.1	2.0	1.9	1.3	0.5	28.4	AlF_6	$AlF_{2.42}(OH)_{0.58}$
	-11.3	3.5	3.6	3.0	1	39.1	$AlF_5(OH)$	
	-8.7	3.7	4.7	3.0	1	20.4	$AlF_4(OH)_2$	*$AlF_{2.39}(OH)_{0.61}$*
	-5.2	3.0	5.5	4.3	0.5	12.3	$AlF_3(OH)_3$	

Table 3. Probabilities of occurrence (%) of the $AlF_{6-y}(OH)_y$ groups, for various $AlF_{3-x}(OH)_x$ chemical compositions, assuming an equal OH content in both Al1 and Al2 sites and based on a OH/F distribution on F1 and F2 sites (probabilities of occurrence of $AlF(OH)_5$ and $Al(OH)_6$ equal to zero) and (in italic) on all F sites (probabilities of occurrence of $Al(OH)_6$ negligible).

Composition	**AlF_6**	**$AlF_5(OH)$**	**$AlF_4(OH)_2$**	**$AlF_3(OH)_3$**	**$AlF_2(OH)_4$**	**$AlF(OH)_5$**
$AlF_{2.5}(OH)_{0.5}$	31.6	42.2	21.1	4.7	0.4	0
	33.5	*40.2*	*20.1*	*5.4*	*0.8*	*0.1*
$AlF_{2.4}(OH)_{0.6}$	24.0	41.2	26.5	7.6	0.8	0
	26.2	*39.3*	*24.6*	*8.2*	*1.5*	*0.2*

Table 4. Probabilities of occurrence (%) of the $FAl_2F_{10-z}(OH)_z$ groups for two $AlF_{3-x}(OH)_x$ chemical compositions, based on a OH/F distribution on F1 and F2 sites (negligible for z = 8, equal to zero for z = 9 and 10) and (in italic) on all F sites (negligible for z = 8, 9 and 10).

Chemical composition	**z = 0**	**z = 1**	**z = 2**	**z = 3**	**z = 4**	**z = 5**	**z = 6**	**z = 7**
$AlF_{2.5}(OH)_{0.5}$	15.2	32.6	30.2	15.7	5.1	1.1	0.1	0.0
	16.2	*32.3*	*29.1*	*15.5*	*5.4*	*1.3*	*0.2*	*0.0*
$AlF_{2.4}(OH)_{0.6}$	9.8	26.8	31.5	20.8	8.5	2.2	0.4	0.0
	10.7	*26.8*	*30.2*	*20.1*	*8.8*	*2.6*	*0.6*	*0.1*

Table 5. Isotropic chemical shifts (δ_{iso}, ppm), line widths (LW, ppm) and relative intensities (I, %) of the six ^{19}F NMR lines used for the fits of the ^{19}F MAS NMR spectra of the five β-$AlF_{3-x}(OH)_x$ samples, and average δ_{iso} (ppm) and assignment of these lines.

	Line	1	2	3	4	5	6
	δ_{iso}	-172.5	-169.3	-165.3	-160.8	-154.5	-149.5
S-25	**LW**	4.9	7.1	7.9	9.7	6.6	6.0
	I	16	32.8	28.8	17.7	3	1.7
	δ_{iso}	-172.8	-170.3	-165.7	-160.7	-154.2	-146.6
S-60	**LW**	4.5	7.4	7.1	7.7	8.0	9.0
	I	17.7	32.4	29.4	12	6.4	2.1
	δ_{iso}	-172.6	-169.5	-165.3	-160.9	-155.1	-149.0
S-185	**LW**	5.0	7.5	7.7	8.6	8.0	6.0
	I	18.7	32.9	28.9	12.7	5.6	1.2
	δ_{iso}	-174.4	-171.2	-166.2	-161.8	-156	-148.4
S-300	**LW**	6.8	5.6	5.9	7.7	9.2	9.5
	I	10.5	28.1	31.8	19.8	7.7	2.1
	δ_{iso}	-173.6	-171.1	-166.1	-161.9	-156	-149.3
S-345	**LW**	7.2	5.7	5.6	7.6	8.6	8.1
	I	10.2	28.7	31.3	20.6	7.9	1.3
$<\delta_{iso}>$		-173.2	-170.3	-165.7	-161.2	-155.2	-148.5
Assignment		FAl_2F_{10}	$FAl_2F_9(OH)$	$FAl_2F_8(OH)_2$	$FAl_2F_7(OH)_3$	$FAl_2F_6(OH)_4$	$FAl_2F_5(OH)_5$

References

(1) Tressaud, A. *Functionalized Inorganic Fluorides: Synthesis, Characterization & Properties of Nanostructured Solids*; Tressaud, A., Ed.; WILEY: Chichester: West Sussex, 2010. https://doi.org/10.1002/9780470660768.

(2) Tressaud, A.; Poeppelmeier, K. R. *Photonic and Electronic Properties of Fluoride Materials: Progress in Fluorine Science Series*, Progress i.; Tressaud, A., Poeppelmeier, K. R., Eds.; Elsevier: Amsterdam, 2016. https://doi.org/10.1016/C2013-0-18987-8.

(3) Nakajima, T.; Zemva, B.; Tressaud, A. *Synthesis, Characterization and Applications*, Amsterdam.; Elsevier: New-York, 2000.

(4) Kemnitz, E.; Menz, D. H. Fluorinated Metal Oxides and Metal Fluorides as Heterogeneous Catalysts. *Progress in Solid State Chemistry* **1998**, *26* (2–3), 97–153. https://doi.org/10.1016/S0079-6786(98)00003-X.

(5) Zheng, J.; Gu, M.; Xiao, J.; Polzin, B. J.; Yan, P.; Chen, X.; Wang, C.; Zhang, J. G. Functioning Mechanism of AlF_3 Coating on the Li- and Mn-Rich Cathode Materials. *Chemistry of Materials* **2014**, *26* (22), 6320–6327. https://doi.org/10.1021/cm502071h.

(6) Luo, Z.; Lei, W.; Wang, X.; Pan, J.; Pan, Y.; Xia, S. AlF_3 Coating as Sulfur Immobilizers in Cathode Material for High Performance Lithium-Sulfur Batteries. *Journal of Alloys and Compounds* **2020**, *812*, 152132. https://doi.org/10.1016/j.jallcom.2019.152132.

(7) Sun, J.; Li, X.; Zhang, W.; Yi, K.; Shao, J. High-Reflectivity Mirrors by Al_2O_3, LaF_3 and AlF_3 for 193 Nm Application. *Optics and Laser Technology* **2014**, *56*, 65–70. https://doi.org/10.1016/j.optlastec.2013.07.017.

(8) Mäntymäki, M.; Heikkilä, M. J.; Puukilainen, E.; Mizohata, K.; Marchand, B.; Räisänen, J.; Ritala, M.; Leskelä, M. Atomic Layer Deposition of AlF_3 Thin Films Using Halide Precursors. *Chemistry of Materials* **2015**, *27* (2), 604–611. https://doi.org/10.1021/cm504238f.

(9) Herron, N.; Farneth, W. E. The Design and Synthesis of Heterogeneous Catalyst Systems. *Advanced Materials* **1996**, *8* (12), 959–968. https://doi.org/10.1002/adma.19960081203.

(10) Mao, W.; Bai, Y.; Jia, Z.; Yang, Z.; Hao, Z.; Lu, J. Highly Efficient Gas-Phase Dehydrofluorination of 1,1,1,3,3-Pentafluoropropane to 1,3,3,3-Tetrafluoropropene over Mesoporous Nano-Aluminum Fluoride Prepared from a Polyol Mediated Sol-Gel Process. *Applied Catalysis A: General* **2018**, *564* (July), 147–156. https://doi.org/10.1016/j.apcata.2018.07.028.

(11) Mao, W.; Bai, Y.; Wang, B.; Wang, W.; Ma, H.; Qin, Y.; Li, C.; Lu, J.; Liu, Z. A Facile Sol-Gel Synthesis of Highly Active Nano A-Aluminum Fluoride Catalyst for Dehydrofluorination of Hydrofluorocarbons. *Applied Catalysis B: Environmental* **2017**, *206*, 65–73. https://doi.org/10.1016/j.apcatb.2016.12.064.

(12) Liu, B.; Han, W.; Chen, A.; Li, L.; Tang, H.; Lu, C.; Zhang, G.; Li, Y.; Li, X. Confinement of AlF_3 in MOF Derived Structures for the Formation of 4-Fold Coordinated Al and Significantly Improved Dehydrofluorination Activity. *Chemical Engineering Journal* **2020**, *394* (March). https://doi.org/10.1016/j.cej.2020.124946.

(13) Park, N. K.; Jeong, Y. H.; Lee, J. W.; Lee, T. J. Catalytic Activity of AlF_3 Nano-Structure for Hydrolysis of NF_3. *Catalysis Today* **2018**, *303* (June 2017), 46–54. https://doi.org/10.1016/j.cattod.2017.09.030.

(14) Daniel, P.; Bulou, A.; Rousseau, M.; Nouet, J.; Fourquet, J. L.; Leblanc, M.; Burriel, R. A Study of the Structural Phase Transitions in AlFNanostructured Aluminium Hydroxyfluorides Derived from β-AlF_3: X-Ray Powder Diffraction, Differential Scanning

Calorimetry (DSC) and Raman Scattering Investigations of the Lattice Dynamics and p. *Journal of Physics: Condensed Matter* **1990**, *2* (26), 5663–5677. https://doi.org/10.1088/0953-8984/2/26/003.

(15) Le Bail, A.; Jacoboni, C.; Leblanc, M.; De Pape, R.; Duroy, H.; Fourquet, J. L. Crystal Structure of the Metastable Form of Aluminum Trifluoride β-AlF_3 and the Gallium and Indium Homologs. *Journal of Solid State Chemistry* **1988**, *77* (1), 96–101. https://doi.org/10.1016/0022-4596(88)90095-3.

(16) Herron, N.; Thorn, D. L.; Harlow, R. L.; Jones, G. A.; Parise, J. B.; Fernandez-Baca, J. A.; Vogt, T. Preparation and Structural Characterization of Two New Phases of Aluminum Trifluoride. *Chemistry of Materials* **1995**, *7* (1), 75–83. https://doi.org/10.1021/cm00049a013.

(17) Delong, X.; Yongqin, L.; Ying, J.; Longbao, Z.; Wenkui, G. Thermal Behavior of Aluminum Fluoride Trihydrate. *Thermochimica Acta* **2000**, *352* (353), 47–52. https://doi.org/10.1016/S0040-6031(99)00436-0.

(18) Rüdiger, S.; Eltanany, G.; Groß, U.; Kemnitz, E. Real Sol-Gel Synthesis of Catalytically Active Aluminium Fluoride. *J Sol-Gel Sci Technol* **2007**, *41* (3), 299–311. https://doi.org/10.1007/s10971-006-9008-0.

(19) Kemnitz, E.; Groß, U.; Rüdiger, S.; Shekar, C. S. Amorphous Metal Fluorides with Extraordinary High Surface Areas. *Angew. Chem. Int. Ed.* **2003**, *42* (35), 4251–4254. https://doi.org/10.1002/anie.200351278.

(20) Shinn, D. B.; Crocket, D. S.; Haendler, H. M. The Thermal Decomposition of Ammonium Hexafluoroferrate(III) and Ammonium Hexafluoroaluminate. A New Crystalline Form of Aluminum Fluoride. *Inorganic Chemistry* **1966**, *5* (11), 1927–1933. https://doi.org/10.1021/ic50045a020.

(21) Baumer, A.; Caruba, R.; Turco, G. Préparation Par Voie Hydrothermale d'un Hydroxyfluorure de Gallium 16 $Ga(OH, F)_3$ Isotype de $Al(OH, F)_3.6\ H_2O$ et d'un Composé Nouveau $Ga(OH, F)_3$ Isotype de $Al(OH, F)_3$. *C. R. Acad. Sc. Paris Serie D* **1971**, *272*, 3105–3108.

(22) Estruga, M.; Meng, F.; Li, L.; Chen, L.; Li, X.; Jin, S. Large-Scale Solution Synthesis of α-AlF3·3H2O Nanorods under Low Supersaturation Conditions and Their Conversion to Porous β-AlF3 Nanorods. *J. Mater. Chem.* **2012**, *22* (39), 20991. https://doi.org/10.1039/c2jm33782g.

(23) Skapin, T.; Tavčar, G.; Benčan, A.; Mazej, Z. Recent Developments in the Preparation of High Surface Area Metal Fluorides. *Journal of Fluorine Chemistry* **2009**, *130* (12), 1086–1092. https://doi.org/10.1016/j.jfluchem.2009.06.015.

(24) Delattre, J. L.; Chupas, P. J.; Grey, C. P.; Stacy, A. M. Plasma-Fluorination Synthesis of High Surface Area Aluminum Trifluoride from a Zeolite Precursor. *Journal of the American Chemical Society* **2001**, *123* (22), 5364–5365. https://doi.org/10.1021/ja015645t.

(25) Štefančič, A.; Primc, D.; Tavčar, G.; Skapin, T. Direct Solvothermal Preparation of Nanostructured Fluoride Aerogels Based on AlF_3. *Dalton Transactions* **2015**, *44* (47), 20609–20617. https://doi.org/10.1039/c5dt03423j.

(26) Dambournet, D.; Demourgues, A.; Martineau, C.; Pechev, S.; Lhoste, J.; Majimel, J.; Vimont, A.; Lavalley, J. C.; Legein, C.; Buzaré, J. Y.; Fayon, F.; Tressaud, A. Nanostructured Aluminium Hydroxyfluorides Derived from β-AlF_3. *Chemistry of Materials* **2008**, *20* (4), 1459–1469. https://doi.org/10.1021/cm702603b.

(27) Dambournet, D.; Demourgues, A.; Martineau, C.; Durand, E.; Majimel, J.; Vimont, A.; Leclerc, H.; Lavalley, J. C.; Daturi, M.; Legein, C.; Buzaré, J. Y.; Fayon, F.; Tressaud, A. Structural Investigations and Acidic Properties of High Surface Area Pyrochlore Aluminium Hydroxyfluoride. *Journal of Materials Chemistry* **2008**, *18* (21), 2483–2492. https://doi.org/10.1039/b718856k.

(28) Yang, C.; Wang, X.; Omary, M. A. Fluorous Metal-Organic Frameworks for High-Density Gas Adsorption. *Journal of the American Chemical Society* **2007**, *129* (50), 15454–15455. https://doi.org/10.1021/ja0775265.

(29) Eriksson, L.; Johansson, E.; Wold, N. K.-; Wikström, C.; Wold, S. Design of Experiments, Principles and Applications. In *Journal of Chemometrics*; Umea : Umetrics, Ed.; WILEY: Stockholm, 2001; pp 495–496.

(30) Rietveld, H. M. A Profile Refinement Method for Nuclear and Magnetic Structures. *Journal of Applied Crystallography* **1969**, *2* (2), 65–71. https://doi.org/10.1107/s0021889869006558.

(31) Rodriguez-Carvajal, J. Magnetic Structure Determination from Powder Diffraction Using the Program *FullProf*. *Applied Crystallography* **2001**, No. 2, 30–36.

(32) Thompson, P.; Cox, D. E.; Hastings, J. B. Rietveld Refinement of Debye-Scherrer Synchrotron X-Ray Data from Al_2O_3. *Journal of Applied Crystallography* **1987**, *20*, 79–83. https://doi.org/10.1142/9789812811325_0005.

(33) Langford, J. I. A Rapid Method for Analysing the Breadths of Diffraction and Spectral Lines Using the Voigt Function. *Journal of Applied Crystallography* **1978**, *11* (1), 10–14. https://doi.org/10.1107/s0021889878012601.

(34) Weingarth, M.; Tekely, P.; Bodenhausen, G. Efficient Heteronuclear Decoupling by Quenching Rotary Resonance in Solid-State NMR. *Chemical Physics Letters* **2008**, *466* (4–6), 247–251. https://doi.org/10.1016/j.cplett.2008.10.041.

(35) Medek, A.; Harwood, J. S.; Frydman, L. Multiple-Quantum Magic-Angle Spinning NMR: A New Method for the Study of Quadrupolar Nuclei in Solids. *Journal of the American Chemical Society* **1995**, *117* (51), 12779–12787. https://doi.org/10.1021/ja00156a015.

(36) Amoureux, J. P.; Fernandez, C.; Steuernagel, S. Z Filtering in MQMAS NMR. *Journal of Magnetic Resonance - Series A* **1996**, *123* (1), 116–118. https://doi.org/10.1006/jmra.1996.0221.

(37) States, D. J.; Haberkorn, R. A.; Ruben, D. J. A 2D Nuclear Overhauser Expt. with Pure Absorption Phase in Four Quadrants. *J. Magn. Reson.* **1982**, *48*, 286–292.

(38) Massiot, D.; Fayon, F.; Capron, M.; King, I.; Le Calvé, S.; Alonso, B.; Durand, J. O.; Bujoli, B.; Gan, Z.; Hoatson, G. Modelling One- and Two-Dimensional Solid-State NMR Spectra. *Magnetic Resonance in Chemistry* **2002**, *40* (1), 70–76. https://doi.org/10.1002/mrc.984.

(39) Okhotnikov, K.; Charpentier, T.; Cadars, S. Supercell Program: A Combinatorial Structure-Generation Approach for the Local-Level Modeling of Atomic Substitutions and Partial Occupancies in Crystals. *J Cheminform* **2016**, *8* (1), 17. https://doi.org/10.1186/s13321-016-0129-3.

(40) Pickard, C. J.; Mauri, F. All-Electron Magnetic Response with Pseudopotentials: NMR Chemical Shifts. *Physical Review B* **2001**, *63* (24). https://doi.org/10.1103/PhysRevB.63.245101.

(41) Profeta, M.; Mauri, F.; Pickard, C. J. Accurate First Principles Prediction of ^{17} O NMR Parameters in SiO $_2$: Assignment of the Zeolite Ferrierite Spectrum. *J. Am. Chem. Soc.* **2003**, *125* (2), 541–548. https://doi.org/10.1021/ja027124r.
(42) Segall, M. D.; Lindan, P. J. D.; Probert, M. J.; Pickard, C. J.; Hasnip, P. J.; Clark, S. J.; Payne, M. C. First-Principles Simulation: Ideas, Illustrations and the CASTEP Code. *J. Phys.: Condens. Matter* **2002**, *14* (11), 2717–2744. https://doi.org/10.1088/0953-8984/14/11/301.
(43) Clark, S. J.; Segall, M. D.; Pickard, C. J.; Hasnip, P. J.; Probert, M. I. J.; Refson, K.; Payne, M. C. First Principles Methods Using CASTEP. *Zeitschrift für Kristallographie - Crystalline Materials* **2005**, *220* (5/6). https://doi.org/10.1524/zkri.220.5.567.65075.
(44) Perdew, J. P.; Burke, K.; Ernzerhof, M. Generalized Gradient Approximation Made Simple. *Physical Review Letters* **1996**, *77* (18), 3865–3868. https://doi.org/10.1103/PhysRevLett.77.3865.
(45) Yates, J. R.; Pickard, C. J.; Mauri, F. Calculation of NMR Chemical Shifts for Extended Systems Using Ultrasoft Pseudopotentials. *Physical Review B* **2007**, *76* (2). https://doi.org/10.1103/PhysRevB.76.024401.
(46) Sadoc, A.; Body, M.; Legein, C.; Biswal, M.; Fayon, F.; Rocquefelte, X.; Boucher, F. NMR Parameters in Alkali, Alkaline Earth and Rare Earth Fluorides from First Principle Calculations. *Physical Chemistry Chemical Physics* **2011**, *13* (41), 18539. https://doi.org/10.1039/c1cp21253b.
(47) Cadars, S.; Guégan, R.; Garaga, M. N.; Bourrat, X.; Le Forestier, L.; Fayon, F.; Huynh, T. V.; Allier, T.; Nour, Z.; Massiot, D. New Insights into the Molecular Structures, Compositions, and Cation Distributions in Synthetic and Natural Montmorillonite Clays. *Chem. Mater.* **2012**, *24* (22), 4376–4389. https://doi.org/10.1021/cm302549k.
(48) Sadoc, A.; Biswal, M.; Body, M.; Legein, C.; Boucher, F.; Massiot, D.; Fayon, F. NMR Parameters in Column 13 Metal Fluoride Compounds (AlF_3, GaF_3, InF_3 and TlF) from First Principle Calculations. *Solid State Nuclear Magnetic Resonance* **2014**, *59–60*, 1–7. https://doi.org/10.1016/j.ssnmr.2014.01.001.
(49) Chupas, P. J.; Ciraolo, M. F.; Hanson, J. C.; Grey, C. P. In Situ X-Ray Diffraction and Solid-State NMR Study of the Fluorination of γ-Al_2O_3 with HCF_2 Cl. *Journal of the American Chemical Society* **2001**, *123* (8), 1694–1702. https://doi.org/10.1021/ja0032374.
(50) Kamalanathan, N.; Shamima, H.; Gopalakrishnan, R.; Vishista, K. Influence of Solvents on Solvothermal Synthesis of Cu_2SnS_3 Nanoparticles with Enhanced Optical, Photoconductive and Electrical Properties. *Materials Technology* **2018**, *33* (2), 72–78. https://doi.org/10.1080/10667857.2017.1376788.
(51) Wuttke, S.; Scholz, G.; Rüdiger, S.; Kemnitz, E. Variation of Sol–Gel Synthesis Parameters and Their Consequence for the Surface Area and Structure of Magnesium Fluoride. *J. Mater. Chem.* **2007**, *17* (47), 4980. https://doi.org/10.1039/b711855d.
(52) Thommes, M.; Kaneko, K.; Neimark, A. V.; Olivier, J. P.; Rodriguez-Reinoso, F.; Rouquerol, J.; Sing, K. S. W. Physisorption of Gases, with Special Reference to the Evaluation of Surface Area and Pore Size Distribution (IUPAC Technical Report). *Pure and Applied Chemistry* **2015**, *87* (9–10), 1051–1069. https://doi.org/10.1515/pac-2014-1117.
(53) Pickering, S. U. Emulsions. *J. Chem. Soc., Trans.* **1907**, *91*, 2001–2021.
(54) Dambournet, D.; Demourgues, A.; Martineau, C.; Majimel, J.; Feist, M.; Legein, C.; Buzaré, J. Y.; Fayon, F.; Tressaud, A. Nanostructured Al-Based Fluoride-Oxide Materials

with a Core-Shell Morphology. *Journal of Physical Chemistry C* **2008**, *112* (32), 12374–12380. https://doi.org/10.1021/jp801310e.

(55) Dambournet, D.; Demourgues, A.; Martineau, C.; Durand, E.; Majimel, J.; Legein, C.; Buzaré, J. Y.; Fayon, F.; Vimont, A.; Leclerc, H.; Tressaud, A. Microwave Synthesis of an Aluminum Fluoride Hydrate with Cationic Vacancies: Structure, Thermal Stability, and Acidic Properties. *Chemistry of Materials* **2008**, *20* (22), 7095–7106. https://doi.org/10.1021/cm8023617.

(56) König, R.; Scholz, G.; Pawlik, A.; Jäger, C.; Van Rossum, B.; Oschkinat, H.; Kemnitz, E. Crystalline Aluminum Hydroxy Fluorides: Structural Insights Obtained by High Field Solid State NMR and Trend Analyses. *Journal of Physical Chemistry C* **2008**, *112* (40), 15708–15720. https://doi.org/10.1021/jp804662f.

(57) Gan, Z.; Gor'kov, P.; Cross, T. A.; Samoson, A.; Massiot, D. Seeking Higher Resolution and Sensitivity for NMR of Quadrupolar Nuclei at Ultrahigh Magnetic Fields. *J. Am. Chem. Soc.* **2002**, *124* (20), 5634–5635. https://doi.org/10.1021/ja025849p.

(58) Chupas, P. J.; Corbin, D. R.; Rao, V. N. M.; Hanson, J. C.; Grey, C. P. A Combined Solid-State NMR and Diffraction Study of the Structures and Acidity of Fluorinated Aluminas: Implications for Catalysis. *Journal of Physical Chemistry B* **2003**, *107* (33), 8327–8336. https://doi.org/10.1021/jp0300905.

(59) Shet, S. P.; Shanmuga Priya, S.; Sudhakar, K.; Tahir, M. A Review on Current Trends in Potential Use of Metal-Organic Framework for Hydrogen Storage. *International Journal of Hydrogen Energy* **2021**, *46* (21), 11782–11803. https://doi.org/10.1016/j.ijhydene.2021.01.020.

(60) Myers, A. L. Thermodynamics of Adsorption in Porous Materials. *AIChE Journal* **2002**, *48* (1), 145–160. https://doi.org/10.1002/aic.690480115.

(61) Seenithurai, S.; Chai, J.-D. Effect of Li Adsorption on the Electronic and Hydrogen Storage Properties of Acenes: A Dispersion-Corrected TAO-DFT Study. *Sci Rep* **2016**, *6* (1), 33081. https://doi.org/10.1038/srep33081.

(62) Sumida, K.; Stück, D.; Mino, L.; Chai, J.-D.; Bloch, E. D.; Zavorotynska, O.; Murray, L. J.; Dincă, M.; Chavan, S.; Bordiga, S.; Head-Gordon, M.; Long, J. R. Impact of Metal and Anion Substitutions on the Hydrogen Storage Properties of M-BTT Metal–Organic Frameworks. *J. Am. Chem. Soc.* **2013**, *135* (3), 1083–1091. https://doi.org/10.1021/ja310173e.

Table of Contents graphic

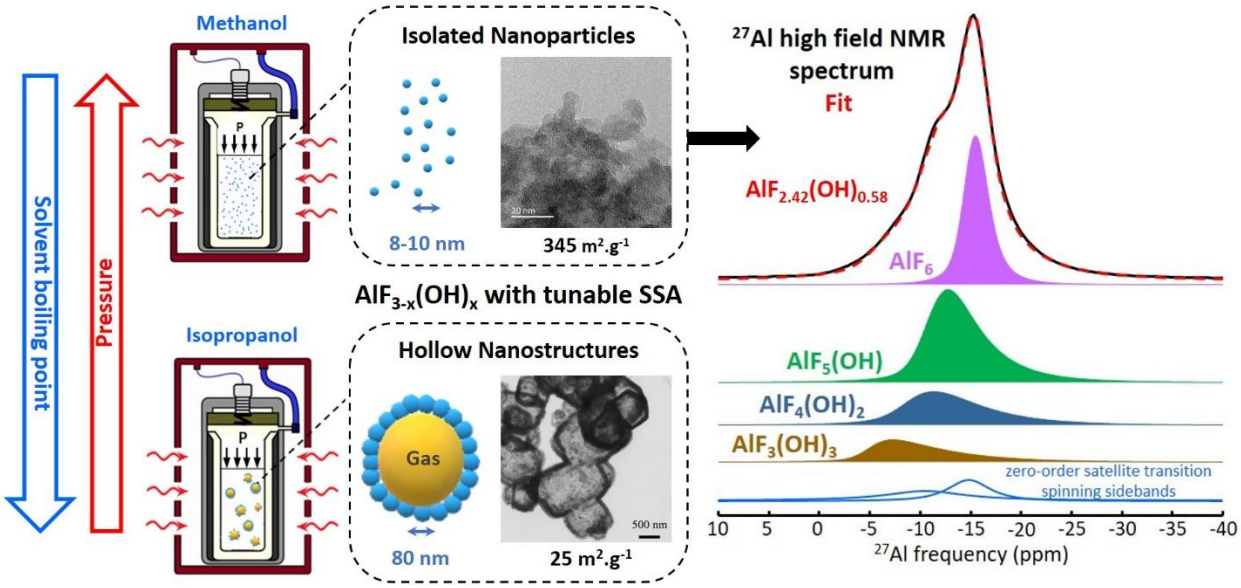

Optimised synthesis allow obtaining β-$AlF_{3-x}(OH)_x$ nanoparticles with specific surface area ranging from 25 to 345 $m^2.g^{-1}$. Their OH contents, estimated using ^{27}Al high-field solid-state NMR which allows to discriminate four resonances assigned to four distinct $AlF_{6-y}(OH)_y$ groups (y = 0 to 3), increase slightly, from ~16% ($AlF_{2.52}(OH)_{0.48}$) to ~ 19% ($AlF_{2.42}(OH)_{0.58}$).